IOP Publishing | International Atomic Energy Agency Nuclear Fusion

Nucl. Fusion **56** (2016) 112011 (15pp) doi:10.1088/0029-5515/56/11/112011

Interpretation of fast-ion signals during beam modulation experiments

W.W. Heidbrink[1], C.S. Collins[1], L. Stagner[1], Y.B. Zhu[1], C.C. Petty[2] and M.A. Van Zeeland[2]

[1] University of California Irvine, Irvine, CA, USA
[2] General Atomics, San Diego, CA, USA

E-mail: Bill.Heidbrink@uci.edu

Received 12 January 2016, revised 4 March 2016
Accepted for publication 9 March 2016
Published 22 July 2016

Abstract

Fast-ion signals produced by a modulated neutral beam are used to infer fast-ion transport. The measured quantity is the divergence of perturbed fast-ion flux from the phase-space volume measured by the diagnostic, $\nabla \cdot \tilde{\Gamma}$. Since velocity-space transport often contributes to this divergence, the phase-space sensitivity of the diagnostic (or 'weight function') plays a crucial role in the interpretation of the signal. The source and sink make major contributions to the signal but their effects are accurately modelled by calculations that employ an exponential decay term for the sink. Recommendations for optimal design of a fast-ion transport experiment are given, illustrated by results from DIII-D measurements of fast-ion transport by Alfvén eigenmodes. The signal-to-noise ratio of the diagnostic, systematic uncertainties in the modeling of the source and sink, and the non-linearity of the perturbation all contribute to the error in $\nabla \cdot \tilde{\Gamma}$.

Keywords: fast-ions, transport analysis, phase-space transport, perturbative experiments, Alfvén eigenmode instabilities

(Some figures may appear in colour only in the online journal)

1. Introduction

Perturbative experiments are an established technique for studies of thermal transport [1, 2]. The perturbation can be an isolated step (as in impurity laser blow-off experiments) but, more commonly, modulated sources such as gas puffs or electron cyclotron heating (ECH) are employed. The modulated response of the plasma provides information about the transport that is unavailable from steady-state measurements alone; for example, in a perturbative study of particle transport, both the diffusion coefficient D and the convective velocity V can be inferred. In many experiments, a control parameter is varied shot-to-shot to study the dependence of perturbative transport on plasma conditions. For example, in a study of electron transport [3], the actuator for the perturbation is one modulated ECH source, the diagnostic that detects the perturbation is an array of electron cyclotron emission detectors that measure electron temperature T_e, and the equilibrium temperature gradient ∇T_e is modified by changing the deposition location of other ECH sources.

A conceptually similar fast-ion experiment was recently conducted on the DIII-D tokamak [4]. A single modulated neutral-beam source is the actuator for the perturbation, various fast-ion diagnostics are the detectors, and the DC power injected by other neutral beam sources is the control parameter that governs the state of the plasma. The purpose of this paper is to provide a general interpretive framework for a perturbative fast-ion experiment such as this one. When compared to thermal-transport experiments, perturbative fast-ion experiments have several similarities but many important differences.

The starting point for both types of studies is a transport equation,

$$\frac{\partial n}{\partial t} + \nabla \cdot \Gamma = S - L, \tag{1}$$

where, in general, n represents a moment of the distribution function (such as the density), Γ is the corresponding flux, S is the source, and L is the sink. Both types of studies assume the perturbation causes a small change to an equilibrium condition so that equation (1) can be linearized,

$$\frac{\partial \tilde{n}}{\partial t} + \nabla \cdot \tilde{\Gamma} = \tilde{S} - \tilde{L}, \tag{2}$$

where a tilde over a variable represents a first-order perturbed quantity. In practice, the validity of this assumption imposes a constraint on the magnitude of the actuator. Larger oscillations in the modulated source produce stronger perturbed signals but strain the validity of the linearity assumption.

The first important difference between thermal and fast-ion studies is in the quantity n. In thermal studies, inter-species collisions are rapid compared to the modulation frequency, so the distribution function is a local Maxwellian. This is not the case for fast ions. By definition, a fast ion is no longer considered part of the distribution function once it thermalizes. The fast-ion distribution function F is a complicated function of multiple variables such as the energy E, pitch with respect to the magnetic field $v_{\|}/v$, and spatial position. These phase-space variables can be represented in various ways but, whatever the choice, $F(X)$ is neither a Maxwellian in velocity space nor a flux function in coordinate space (Here X represents the chosen phase-space variables.). As a result of this complexity, fast-ion measurements defy simple interpretation. Each diagnostic has its own phase-space sensitivity or 'weight function' $W(X)$ [5–8]. With many simultaneous measurements, use of these weight functions enables tomographic reconstructions of the fast-ion distribution function [9–11]. But no diagnostic measures the fast-ion density directly.

In both thermal and fast-ion studies, the transport equation (equation (2)) is derived from a kinetic equation by integrating over relevant phase-space variables. For example, in a study of thermal particle transport, the kinetic equation is integrated by $\int \mathrm{d}\vec{v}$, $\tilde{n}$ is the perturbed particle density, and equation (2) is the continuity equation. For fast ions, one integrates the kinetic equation by $\int W\,\mathrm{d}X$ to obtain equation (2). The quantity $\tilde{n}$ is the perturbed signal (in the usual diagnostic units such as neutrons s^{-1}); it represents a quantity that is proportional to the density of fast ions in the portion of phase space interrogated by the diagnostic.

The second important difference between thermal and fast-ion studies involves the divergence term in the transport equation, $\nabla \cdot \tilde{\Gamma}$. In their review of thermal perturbative experiments, Ryter *et al* [2] simplify equation (1) to

$$\frac{\partial y}{\partial t} = -\nabla \Gamma + S - L, \tag{3}$$

assuming that radial variations ∇y across flux surfaces are the sole cause of changes in the measured quantity y (In [2], y is equivalent to $\tilde{n}$ and ∇ is the ordinary spatial gradient.). This simplification is incorrect for fast ions. In general, $\nabla \cdot \tilde{\Gamma}$ can change due to transport within the interrogated phase-space volume in any direction: energy, pitch, and space. For example, neutral-particle analyzer (NPA) diagnostics have weight functions that are very narrow in pitch. One can easily imagine a wave-particle interaction that scatters fast ions in pitch, causing a large change in NPA signal. This process has no counterpart in thermal transport studies, where rapid inter-species collisions cause the distribution function to be isotropic in angle. The velocity-space dependence of the flux is also important in experiments that utilize radio-frequency heating to perturb the distribution function of a super-thermal electron [12] or ion population.

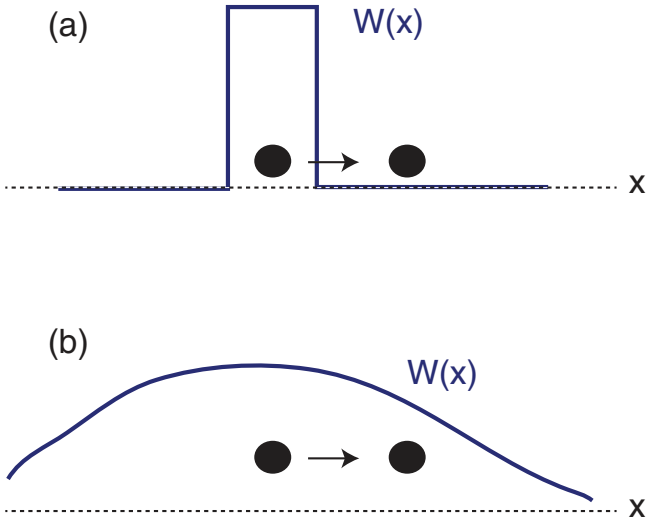

Figure 1. (*a*) For the case of a diagnostic with a narrow weight function, the divergence of the flux is positive when ions leave the interrogated volume. (*b*) For the case of a diagnostic with a broad weight function, the divergence of the flux is positive when ions move to a region of smaller W.

In some cases, the fast-ion diagnostic weight function interrogates a small volume in phase space. In this case, $\nabla \cdot \tilde{\Gamma}$ increases when ions exit the volume and decreases when they enter, as in a canonical illustration of divergence in a mathematics textbook (figure 1(*a*)). However, many diagnostic weight functions change gradually in phase space. In this case, whenever ions move in the direction of decreasing W, (i.e. $\tilde{\Gamma} \cdot \nabla W < 0$) the divergence is positive, even though the ion remains in the interrogated volume (figure 1(*b*)). This subtlety must be borne in mind throughout the paper. In the following, statements like 'flux from the phase-space volume interrogated by the diagnostic' should be understood to include 'motion to a less heavily weighted portion of phase space'.

Owing to this greater complexity of interpretation, two important insights concerning thermal perturbative experiments are of limited utility in fast-ion studies. One key insight is that different transport 'channels' such as density and temperature are coupled [13]. From the fast-ion perspective, reduction of F to low-order moments such as density and temperature is already an oversimplification. Another key insight in thermal studies is that perturbative experiments permit separate determination of the diffusion and convection coefficients D and V. For fast ions, since the measured $\nabla \cdot \tilde{\Gamma}$ is rarely across spatial coordinates alone, expressing the flux as $\Gamma = -D\nabla n + Vn$ is potentially misleading.

In many thermal transport studies the source and sink terms in equation (2) are negligible. This is rarely the case for a perturbative fast-ion experiment.

An important similarity is in the diagnostic requirements. As Lopes Cardozo observed [1], 'In principle an absolute or even relative calibration is not required, but good temporal

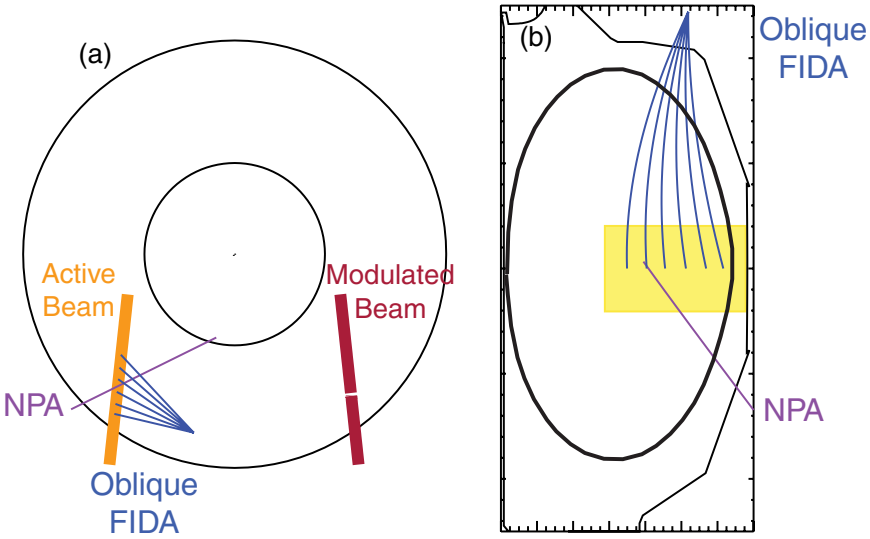

Figure 2. (*a*) Plan view and (*b*) elevation of the DIII-D tokamak, showing the sightlines of the FIDA and NPA diagnostics and the locations of the active and modulated beam. The oval plasma shape utilized in the experiment is also shown. The shaded area in (*b*) represents the vertical height of the injected neutral beam.

and spatial resolution are prerequisite. This is in contrast to steady-state analysis, which requires no time resolution, but for which absolute calibration is essential'. Because relative measurements are generally easier to obtain than absolute measurements, this is an important advantage of the perturbative technique. For fast-ion experiments, good temporal resolution is essential but the requirement of good spatial resolution is replaced by a requirement for accurate knowledge of the phase-space sensitivity of the diagnostic.

The purpose of this paper is to provide a rigorous framework for the interpretation of fast-ion data from perturbative experiments. Section 2 briefly describes the DIII-D experiments that provide examples in the subsequent sections. Section 3 addresses the proper treatment of the source and sink terms. Section 4 explains how to calculate $\nabla \cdot \tilde{\Gamma}$ and the dependence of the results on the modulation frequency and selected source. Section 5 assesses the dependence of the uncertainty on systematic and random errors. The concluding section summarizes the results and provides guidance for a successful perturbative fast-ion experiment.

2. DIII-D Alfvén eigenmode (AE) experiment

As the DIII-D AE experiment is described elsewhere [4], only the details most relevant to the presented data are described here.

The experiment is conducted in the DIII-D tokamak (figure 2). DIII-D is equipped with eight deuterium neutral-beam sources. The actuator for the perturbation is one 70 keV source that is modulated at frequencies between 10–42 Hz. In all but one case, the modulated source injects tangentially off-axis in the direction of the plasma current. Another source acts as an active diagnostic beam, constantly injecting 70 keV neutrals for use by a fast-ion D-alpha (FIDA) diagnostic that views the plasma at an angle of ~45° [14] and a solid-state neutral-particle analyzer that is operated in current mode [15]. Scintillators [16] measure the neutron rate produced by predominately beam-plasma reactions. Injection of other neutral-beam sources changes the average injected power shot-to-shot. The variations in beam power alter the virulence of AE activity (figure 3). When only the modulated and active beam are injected, the level of AE activity is very low; the level of instability-induced transport is considered negligible in these discharges.

The experiment is conducted early in the discharge during the plasma-current ramp (figure 4(*a*)). In the lowest-power discharges, apart from a rare pulse of an additional beam for diagnostic purposes, only the modulated and active beam inject (figure 4(*b*)). The electron density initially rises quickly but changes more slowly after 500 ms (figure 4(*c*)). The neutron, NPA, and FIDA signals respond to the modulated source (figures 4(*d*)–(*f*)). Although the plasma is not perfectly stationary, beam pulses between 500–900 ms are conditionally averaged to obtain an improved signal-to-noise ratio.

3. Source and sink

The ultimate goal of the analysis is to infer $\nabla \cdot \tilde{\Gamma}$ in discharge conditions where, due to transport by instabilities, the divergence of the flux is non-zero. Rearrangement of equation (2) gives

$$\nabla \cdot \tilde{\Gamma} = -\frac{\partial \tilde{n}}{\partial t} + \tilde{S} - \tilde{L}. \tag{4}$$

Since $\tilde{n}$ is the perturbed signal (e.g. in neutrons s^{-1}), the first term on the RHS is measured. The challenge is to determine the source and sink terms, $\tilde{S}$ and $\tilde{L}$. Since the perturbing beam is modulated as a square wave, temporally $\tilde{S} = \pm\tilde{S}_0$, where the plus sign refers to the first half of the cycle and the minus sign to the second half. (Note that the perturbed, first-order, quantities are relative to the *average* (zero-order) quantities so the modulated square wave is both positive and negative.)

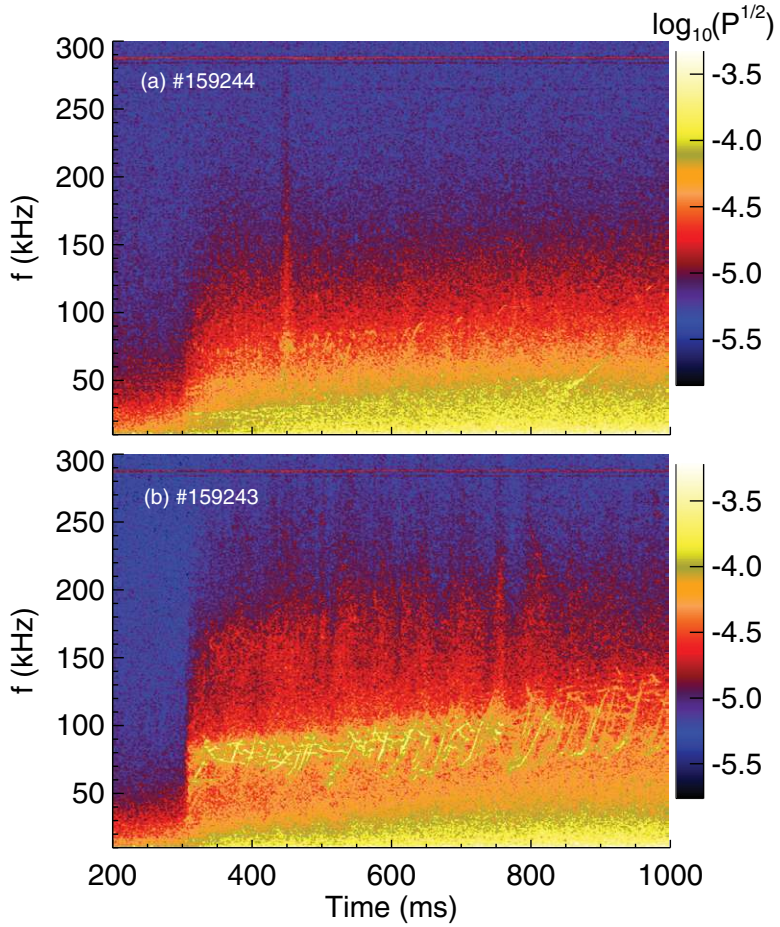

Figure 3. Cross-power of two CO_2 interferometer signals in discharges with an average injected beam power of (*a*) 2.4 MW and (*b*) 6.4 MW.

The magnitude of $\tilde{S}_0$ depends upon the beam deposition of the modulated source and the diagnostic weight. The sink term $\tilde{L}$ is determined by the rate at which Coulomb and atomic collisions extract fast ions from the phase-space volume interrogated by the diagnostic.

Strachan *et al* [17] observed that, after beam injection, the neutron rate decayed exponentially over two orders of magnitude. This motivated introduction of a diagnostic-weighted slowing-down time τ_n,

$$\tau_n = \frac{\tau_{se}}{3} \ln\left[\frac{W_b^{3/2} + W_c^{3/2}}{W_n^{3/2} + W_c^{3/2}}\right], \tag{5}$$

where τ_{se} is the slowing-down time on electrons, W_b is the injection energy, W_c is the critical energy where drag on thermal electrons equals drag on thermal ions, and W_n is the energy where the $d-d$ fusion reactivity has fallen to $1/e$ of its value at W_b. The weighted decay time is shorter than the slowing-down time because, owing to the steep fusion reaction cross section, a fast ion need not slow down to $1/e$ of its initial velocity to reduce the neutron rate to $1/e$ of its initial value. Experiments with beam blips in MHD-quiescent plasmas have confirmed that this model is an excellent description of the effect of thermalization on the neutron signal; see, for example, [18]. For neutron diagnostics, the diagnostically-weighted loss term is accurately approximated by $\tilde{L} \simeq \tilde{n}/\tau_n$.

Inspired by these neutron results, we explore whether this simple decay term can describe the signals produced by a wider variety of diagnostics. Assuming square-wave modulation and $\tilde{L} = \tilde{n}/\tau$, in the absence of instability-induced transport, the modulated signal satisfies the ordinary differential equation

$$\frac{\mathrm{d}\tilde{n}}{\mathrm{d}t} = \begin{cases} \tilde{S}_0 - \dfrac{\tilde{n}}{\tau} & \text{for } 0 < t < T/2 \\ -\tilde{S}_0 - \dfrac{\tilde{n}}{\tau} & \text{for } T/2 < t < T \end{cases} \tag{6}$$

Here, T is the modulation period. The solution to equation (6) that is continuous at $t = 0$ and $t = T/2$ is

$$\tilde{n} = \begin{cases} \tilde{S}_0\tau + a_+ \exp(-t/\tau) & \text{for } 0 < t < T/2 \\ -\tilde{S}_0\tau + a_- \exp(-t/\tau) & \text{for } T/2 < t < T, \end{cases} \tag{7}$$

where

$$\begin{aligned} a_- &= \frac{2\tilde{S}_0\tau}{b}\frac{1-b}{1-b^2}, \\ a_+ &= -ba_-, \\ b &= \exp(-0.5T/\tau). \end{aligned}$$

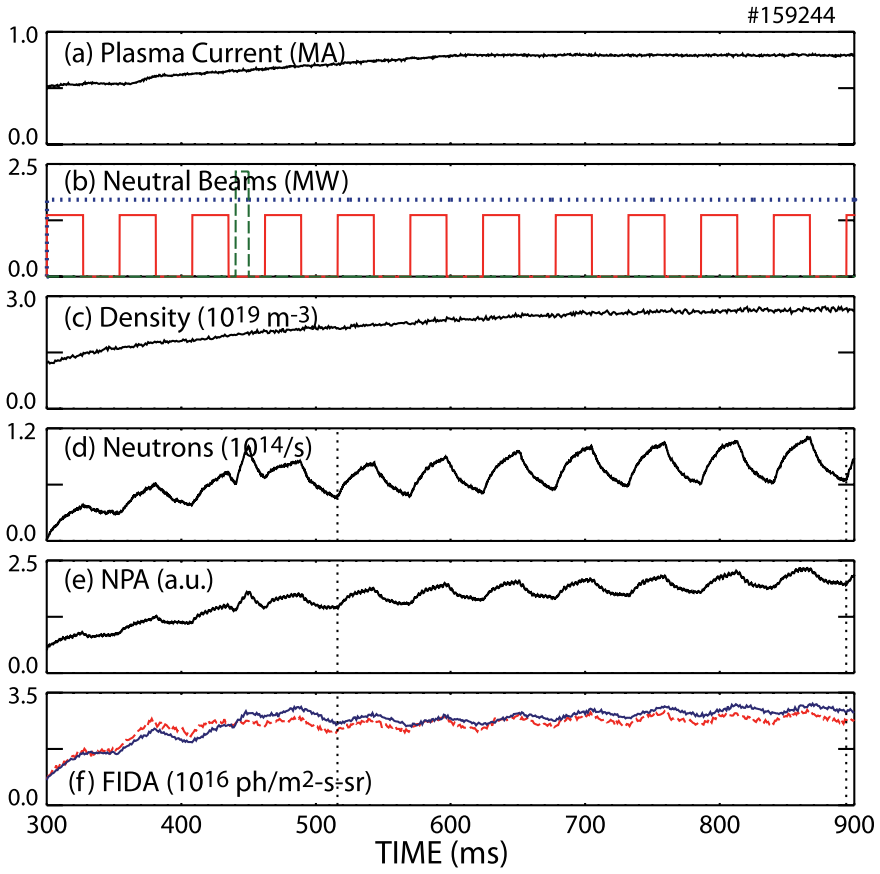

Figure 4. (*a*) Plasma current, (*b*) neutral beam waveforms for the active (dotted), modulated (solid), and additional (dashed) beam, (*c*) line-averaged electron density, (*d*) neutron rate, (*e*) NPA signal, and (*f*) FIDA signals from $R = 1.91$ m (solid) and $R = 2.12$ m (dashed) (after averaging between 651.8–653.3 nm) in a discharge with minimal AE activity. The dotted vertical lines indicate the time window for conditional averaging.

Figure 5 shows conditionally-averaged neutron, NPA, and FIDA signals from a low-power shot. Overlaid on the signals are fits to the data using the functional form of equation (7). The fits are excellent in all cases, justifying the assumed form of the sink term $\tilde{L} = \tilde{n}/\tau$. Also overlaid on the figures are predictions of the evolution based on the distribution function calculated by the TRANSP NUBEAM code [19]. The agreement is also excellent for all signals. A special procedure is employed in these TRANSP calculations. To utilize efficiently the Monte Carlo tracers in the calculation of the modulated beam, all other beams are turned off in the simulation and a relatively large number of markers (10^6) are used. The TRANSP distribution function is averaged over 2 ms and dumped every 3 ms for the same 378 ms interval as the data. The neutron prediction uses the internal TRANSP calculation of the neutron rate, while the NPA and FIDA signals are predicted by 127 FIDASIM [20] calculations. The predicted signals are then conditionally averaged in the same manner as the data. The excellent agreement between experiment and theory validates the assumption that Coulomb and atomic collisions alone provide an adequate description of the evolution of the distribution function in this low-power shot.

The differences between the modelled signals are also instructive. The fitted values of τ are 11, 10, 680, and 16 ms for the neutron, NPA, FIDA channel at $\rho = 0.30$, and the FIDA channel at $\rho = 0.67$, respectively (Here, ρ is the normalized square root of the toroidal flux.). In comparison, the slowing-down time τ_s for a 75 keV ion at the magnetic axis is 35 ms. The differences in the fitted decay times reflect differences in the energy dependence of the diagnostic weight functions. As shown in figure 5(*a*), the neutron and NPA weight functions decrease rapidly with decreasing energy and have similar slopes, so their decay times are much shorter than τ_s and have similar values. In contrast, owing to the energy dependence of the charge-exchange cross sections, from the perspective of a decelerating fast ion, the FIDA weight functions initially increase with decreasing energy, reaching a maximum at ~40 keV. The consequence of this is that the decay time is much longer than τ_s for the FIDA channel at normalized minor radius of $\rho = 0.3$; essentially, the sink is irrelevant on the timescale of the beam modulation and the waveform is a triangle function (figure 5(*d*)). For the FIDA channel at $\rho = 0.6$, the slowing-down time is a factor of two shorter than at $\rho = 0.3$, so the sink does have an effect and the decay time is close to the slowing-down time. The correspondence between the waveform shapes and the weight-function dependencies nicely illustrate the importance of the weight function in the proper interpretation of the signals.

The solution to equation (6) is periodic. In practice, in an actual experiment, the DC levels of the measured signals often evolve gradually; for example, the average values of the neutron, NPA, and FIDA signals in figures 4(*d*)–(*f*) steadily

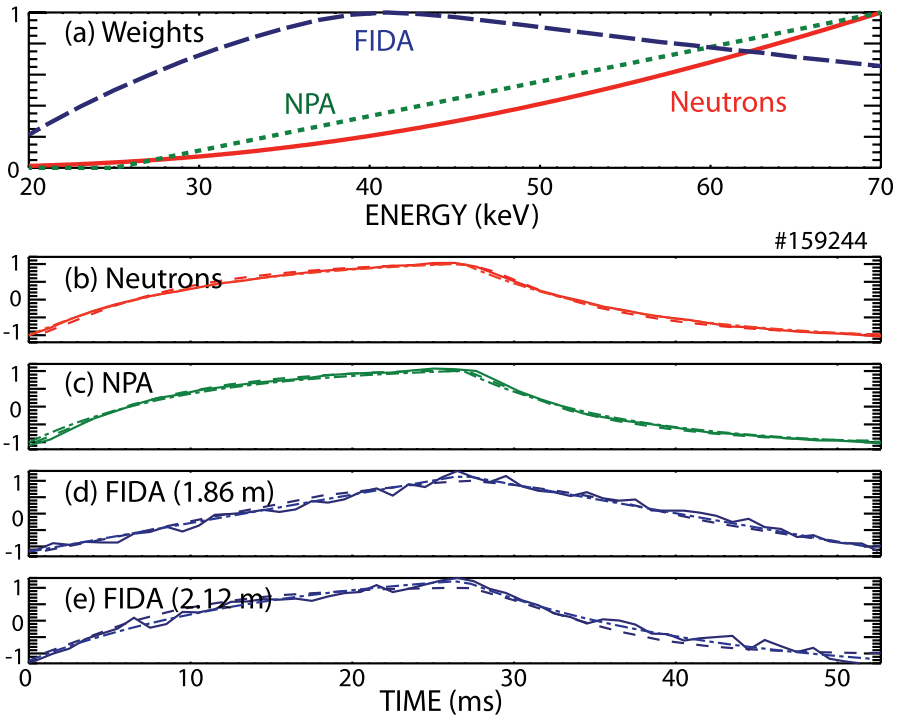

Figure 5. (*a*) Energy dependence of the neutron (solid), NPA (dotted), and FIDA (dashed) weight functions after integration over pitch and space. Detrended and conditionally-averaged (*b*) neutron, (*c*) NPA, (*d*) FIDA at $R = 1.86$ m, and (*e*) FIDA at $R = 2.12$ m signals for the low-power discharge shown in figure 4. The solid lines are experiment, the dashed lines are calculated by TRANSP and FIDASIM, and the dash–dot lines are the fit to equation (7) (Note: the lines are virtually indistinguishable).

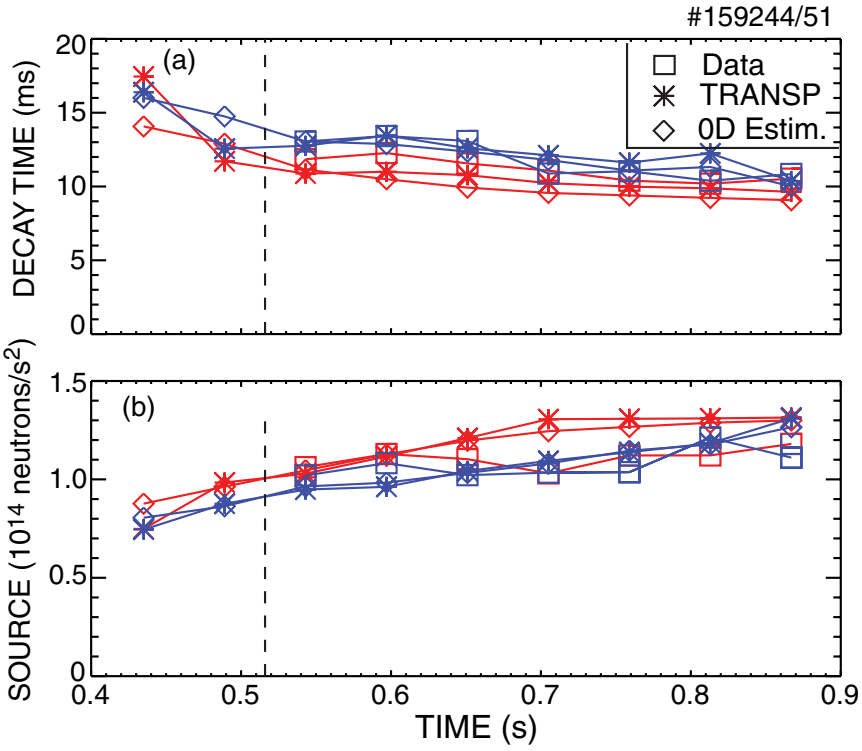

Figure 6. Time evolution of (*a*) τ and (*b*) $\tilde{S}_0$ for the neutron signals in two nominally identical low-power discharges. For the data (□) and TRANSP (∗), the points are from fits to equation (7). The zero-dimensional estimates are from equations (5) and (8), respectively.

increase between 500–900 ms. If one fails to correct for this effect, the conditionally averaged signals are asymmetric and the fit to the model solution (equation (7)) is degraded. The remedy for this effect is to detrend the signals prior to conditional averaging. A low order polynomial is usually employed but, in principle, an exponential rise or decay could also serve as the detrending function. The detrending function should contain only low-frequency components that are well

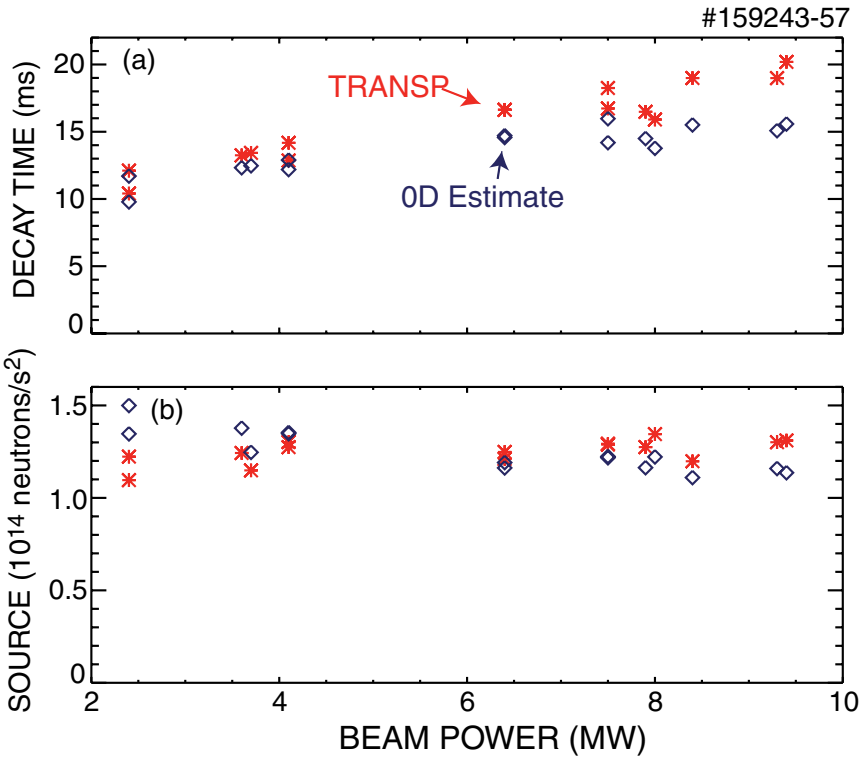

Figure 7. Calculations of (a) τ and (b) $\tilde{S}_0$ for a power scan in the DIII-D AE experiment. The TRANSP points ($*$) are from fits to the predicted signal in the absence of fast-ion transport and the zero-dimensional estimates ($\Diamond$) are from equations (5) and (8), respectively.

below the perturbation frequency. Essentially, the detrending correction acts as a high-pass filter for the data. In this paper, all conditionally averaged signals have had a linear fit to the data subtracted prior to averaging.

Of course, if the plasma is not truly stationary, the AC response of the plasma to the perturbation also evolves. Figure 6 shows the actual evolution of the fit parameters τ and $\tilde{S}_0$ for individual pulses in the discharge that is conditionally averaged in figure 5. There is a conflict between the desire to maximize the number of perturbative cycles, which improves the signal-to-noise ratio, and the desire to minimize the duration of the experiment, which improves the approximation of stationarity. In our analysis of the DIII-D AE experiment, we typically average seven full cycles between 0.5–0.9 s.

The fitted source and sink parameters $\tilde{S}_0$ and τ have simple physical interpretations. To illustrate this, figure 6 compares $\tilde{S}_0$ and τ with zero-dimensional (0D) estimates. For τ, an estimate of the expected value is given by equation (5), evaluated using the average values of T_e and n_e over the inner 2/3 of the plasma. The gradual decay in τ in time (figure 6(a)) is due to the gradual rise in density (figure 4(c)). The good agreement between the 0D estimate and the TRANSP calculation confirms that the dominant physics is the cross-section weighted slowing-down time. The good agreement between the TRANSP and experimental values of τ indicates that $\tilde{L} = \tilde{n}/\tau$ is an adequate model for the thermalization sink.

The source term for the neutron signal is associated with beam-plasma reactions between the beam ions produced by the modulated beam and the thermal deuterium, so a 0D estimate of the source term is

$$\tilde{S}_0 \propto n_d \langle \sigma v \rangle, \tag{8}$$

where n_d is the thermal deuterium density and $\langle \sigma v \rangle$ is the fusion reactivity, including corrections for the plasma rotation and ion temperature. After normalization, this estimate agrees well with the fit to the TRANSP waveform (figure 6(b)), confirming that equation (8) contains the dominant physics. The source term gradually increases in time primarily because the deuterium density n_d is increasing.

In the DIII-D AE experiment, the control parameter is the average injected power, which is scanned shot-to-shot. During the course of this scan, modest changes in plasma profiles occur. Figure 7 compares the values of τ and $\tilde{S}_0$ from fits to the TRANSP neutron waveforms with the 0D analytic estimates. The density, which was feedback controlled, is very similar in all of the discharges in this scan. The electron temperature increases as the power increases, which results in an increase in τ with increasing beam power (figure 7(a)). The near constancy in n_e results in nearly constant values of the source (figure 7(b)). Because the plasma profiles evolve with power, the agreement between the 0D estimates and the more accurate TRANSP prediction is only fair. In evaluation of the divergence of the flux (section 4), the TRANSP calculation should be employed.

4. Divergence of the flux

When instabilities cause fast-ion transport, the measured signals deviate from the model response, equation (7). Through equation (4), the difference between the measured and

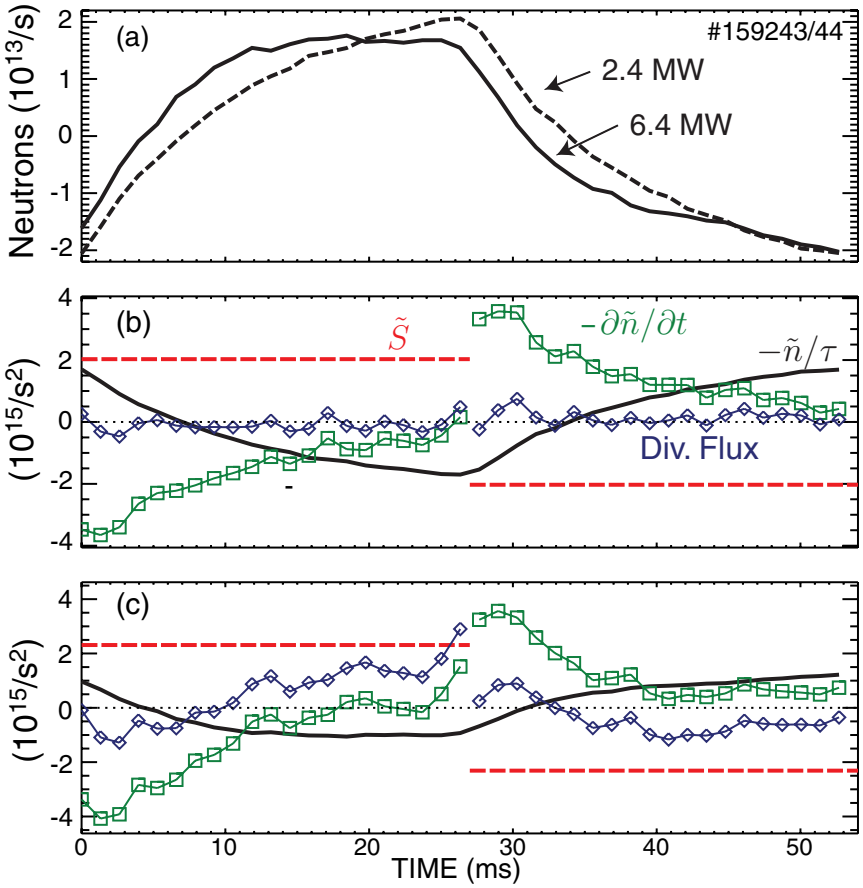

Figure 8. (*a*) Detrended and conditionally-averaged experimental neutron signal in a low-power reference discharge (dashed) and in a discharge with substantial AE activity (solid). (*b*) The terms in equation (9), $\tilde{S}$, $-\partial\tilde{n}/\partial t$, $-n/\tau$, and $\nabla\cdot\tilde{\Gamma}$, in the low-power shot. (*c*) The terms in equation (9) in the high-power shot.

expected signals is used to infer the divergence of flux from the phase-space volume measured by the diagnostic. With the source and sink terms replaced by the terms developed in section 3, equation (4) becomes

$$\nabla\cdot\tilde{\Gamma} = -\frac{\partial\tilde{n}}{\partial t} \pm \tilde{S}_0 - \tilde{n}/\tau. \tag{9}$$

In principle, the terms $\tilde{S}_0$ and τ can be determined by calculation alone but any error in the absolute calibration of the diagnostic will propagate into $\tilde{S}_0$ and impact the inferred $\nabla\cdot\tilde{\Gamma}$. Similarly, errors in the absolute calibration of the electron temperature and density diagnostics can alter τ and hence $\nabla\cdot\tilde{\Gamma}$. If a reference shot with negligible transport is available, it should be used to normalize the calculated source and decay time. The value of $\tilde{S}_0$ used to analyze the discharge with fast-ion transport is

$$\tilde{S}_0 = \frac{\sum|\, y^{\rm exp}_{\rm reference}|}{\sum|\, y^{\rm theory}_{\rm reference}|}\tilde{S}_0^{\rm theory}, \tag{10}$$

where y is the conditionally-averaged signal. The utilized value of τ is

$$\tau = \frac{\tau^{\rm exp}_{\rm reference}}{\tau^{\rm theory}_{\rm reference}}\tau^{\rm theory}. \tag{11}$$

Since low-power reference shots are available for the DIII-D AE experiments, the normalizations of equations (10) and (11) are employed here.

Figure 8 shows analysis of a typical case. The neutron signal in the low-power reference shot agrees well with the waveform predicted by equation (7) but the signal in the 6.4 MW shot with appreciable AE activity differs markedly from the classical prediction. As a check on the calculation, figure 8(*b*) shows the various terms in the equation for the low-power case; as expected, the inferred $\nabla\cdot\tilde{\Gamma}\simeq 0$. Figure 8(*c*) shows the various terms in the equation for the high-power case. At the beginning of the positive cycle, the measured waveform rises more *rapidly* than expected; the corresponding negative value of $\nabla\cdot\tilde{\Gamma}$ during this initial phase means that ions are flowing into the phase-space volume measured by the neutron diagnostic during this phase. By 10 ms, the situation has reversed: the measured waveform increases more slowly than expected so $\nabla\cdot\tilde{\Gamma} > 0$, implying a loss of fast ions from the phase-space volume measured by the diagnostic. (In other words, negative $\nabla\cdot\tilde{\Gamma}$ means ions are moving into regions where the diagnostic weight function is larger; positive $\nabla\cdot\tilde{\Gamma}$ means ions are moving into regions where W is smaller.) For small perturbations, the second half of the cycle with a negative source should be a mirror image of the first half. This is approximately true, with a positive value of $\nabla\cdot\tilde{\Gamma}$ immediately

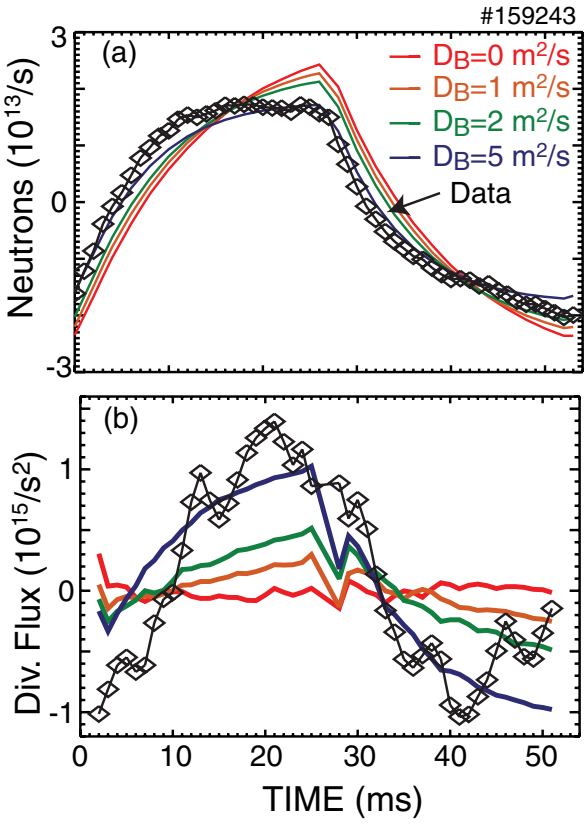

Figure 9. (*a*) Measured (◊) and simulated detrended and conditionally averaged neutron signals in the same discharge as figure 8(*c*). The simulated neutron signals (from largest amplitude to smallest) are from TRANSP runs with spatially constant fast-ion diffusion of 0, 1, 2, and 5 m^2 s^{-1}, respectively. (*b*) Corresponding values of $\nabla \cdot \tilde{\Gamma}$ for the measured and simulated signals.

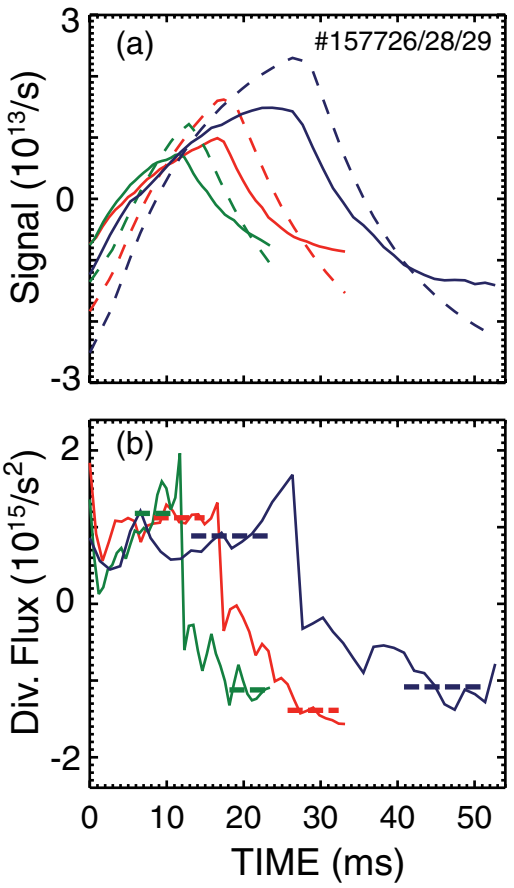

Figure 10. (*a*) Measured (solid) and classically-expected (dashed) detrended and conditionally-averaged neutron signals in nearly identical discharges with three different modulation periods. (*b*) Inferred $\nabla \cdot \tilde{\Gamma}$.

after the beam turns off but a negative value of $\nabla \cdot \tilde{\Gamma}$ in the latter portion of the cycle.

In the DIII-D AE experiment, the inferred $\nabla \cdot \tilde{\Gamma}$ usually asymptotes towards a steady value in the latter halves of the positive and negative cycles. This is not expected in general. The temporal behavior of $\nabla \cdot \tilde{\Gamma}$ contains information about the mechanism of fast-ion transport in the portion of phase space interrogated by the diagnostic. To illustrate this point, special TRANSP runs are conducted with spatially constant ad hoc diffusion D_B and the signals are analyzed in the same manner as the experimental data. Figure 9 shows the result. With increasing diffusion, the signals retain shapes similar to the no-diffusion case but the amplitude of the oscillation is reduced (figure 9(*a*)). As expected, the inferred $\nabla \cdot \tilde{\Gamma}$ increases in magnitude with increasing D_B (figure 9(*b*)) and the negative cycle is a mirror image of the positive cycle. However, in contrast to the experimental $\nabla \cdot \tilde{\Gamma}$ for this discharge, the modelled $|\nabla \cdot \tilde{\Gamma}|$ increases steadily through both the positive and negative cycles. Evidently, the AE-induced transport is roughly 5 m^2 s^{-1} in magnitude but cannot be described by spatially uniform diffusion.

The frequency of the modulated source is selected by the experimenter. Figure 10 compares measurements for different source frequencies in nominally identical shots. The average amplitude of coherent AEs and the average number of AEs only varies 3% and 1% respectively for the scan shown in figure 10. For modulation periods of 24, 34, and 54 ms, the $\nabla \cdot \tilde{\Gamma}$ asymptotes to nearly the same value (to within ∼20%) for the three different periods. Apparently, for the AE-induced transport process, the results are insensitive to the selected period. This is not a general result, however. Simulations of the same discharges with spatially-constant fast-ion diffusion of $D_B = 5$ m^2 s^{-1} yield a value of $\nabla \cdot \tilde{\Gamma}$ that steadily increases with increasing period, as in figure 9(*b*).

The results depend upon the portion of phase space populated by the source. One discharge in the sequence of shots shown in figure 10 used an on-axis, near-perpendicular source rather than the off-axis, near-tangential source employed on every other shot. Figure 11 compares $\nabla \cdot \tilde{\Gamma}$ in these two otherwise identical discharges. The results are quite different for the two cases, especially for the NPA. The NPA weight function only interrogates a small region of phase space, so it is not surprising that the measured divergence depends sensitively upon the phase-space distribution of the source. In a well-designed fast-ion experiment, it is desirable to use different modulated sources to gain information about which portions of phase space experience strong transport and which experience weaker transport.

Two popular analysis techniques for thermal perturbative experiments are of limited utility for fast ions. Typically, the

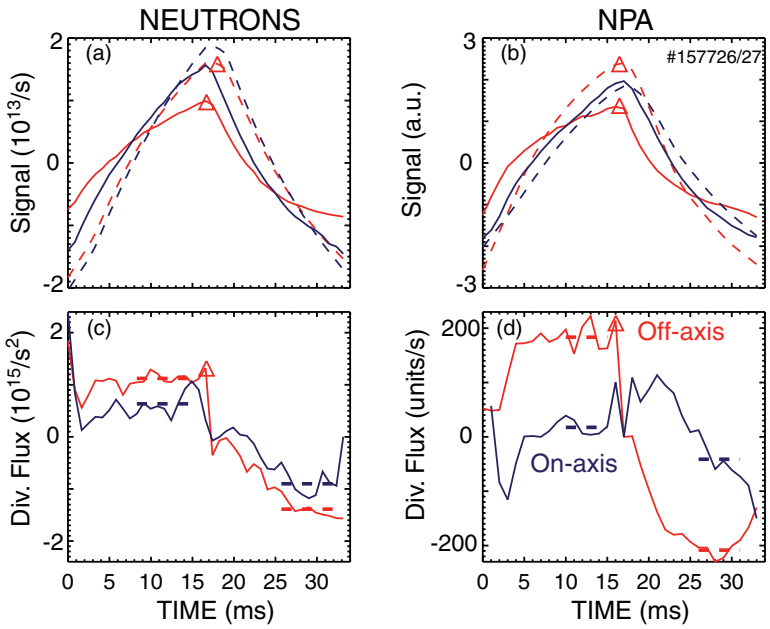

Figure 11. Measured (solid) and classically-expected (dashed) detrended and conditionally-averaged (*a*) neutron and (*b*) NPA signals in nearly identical discharges with different modulated source beams. Curves marked by triangles are from a discharge with a near-tangential off-axis beam, while unmarked curves are from a discharge with a near-perpendicular on-axis beam. (*c*) Neutron and (*d*) NPA $\nabla \cdot \tilde{\Gamma}$ inferred from the signals in the upper panels.

data from a radial array of detectors $\nabla \cdot \tilde{\Gamma}$ is converted into $\tilde{\Gamma}$ by integration over the radius. To implement this for fast ions, the first step is to correct the data for any radial dependence of the weight function. One divides the previously defined $\tilde{\Gamma}$ by the weight function W to obtain a signal that is proportional to the fast-ion flux alone, $\tilde{\gamma} = \tilde{\Gamma}/\int W \, \mathrm{d}X$. This corrects, for example, for attenuation of the injected neutral beam in an active beam diagnostic. Figure 12(*a*) shows a measured FIDA profile of $\nabla \cdot \tilde{\gamma}$. The next step in the putative analysis is to assume that $\nabla \cdot \tilde{\gamma} \simeq (\partial \tilde{\gamma}/\partial R)$ and employ the trapezoidal rule so that the flux $\tilde{\gamma}_R$ at position R is

$$\tilde{\gamma}_R - \tilde{\gamma}_0 \simeq \frac{1}{2} \sum_{i=0}^{N} [(\nabla \cdot \tilde{\gamma})_{i+1} + (\nabla \cdot \tilde{\gamma})_i](R_{i+1} - R_i), \quad (12)$$

where $\tilde{\gamma}_0$ is the flux at the initial position, $(\nabla \cdot \tilde{\gamma})_i$ is the measurement at position i, and $R_{i+1} - R_i$ is the channel-to-channel spacing. There are three challenges with implementation of this procedure for fast ions.

1. It is unclear what to choose for the reference position. In thermal analysis, it is often appropriate to assume zero flux at the magnetic axis. But the fast-ion distribution function is not a flux function. Indeed, for the data in figure 12(*a*), the measured divergence is non-zero at the magnetic axis ($R \simeq 1.72$ m) in this discharge.
2. The signal-to-noise ratio is inadequate to infer the flux accurately through equation (12). Although this deficiency could be remedied with improved fast-ion diagnostics, the quality of the present data is poor compared to a 40–60 channel ECE measurement of $\tilde{T}_e$, for example.
3. The assumption that $\nabla \cdot \tilde{\gamma} \simeq \partial \tilde{\gamma}/\partial R$ is dubious. Figure 12(*b*) shows the velocity-space dependence of the FIDA weight function for one of the FIDA channels. The velocity-space dependence of the other channels is similar. Velocity-space gradients are sharp. Changes in signal can be caused by radial transport but, in a wave-particle interaction, it is equally likely that the signal will change due to changes in energy or pitch.

Another popular analysis technique for thermal perturbative experiments is Fourier analysis of the signals. In Fourier space, algebraic expressions exist for the diffusion and convection coefficients D and V in terms of the amplitude and phase of the perturbation [21]. The dependence of the results on harmonic number are a useful check on the validity of the assumptions. Unfortunately, this approach is most useful in source-free regions, a condition that is violated in our DIII-D AE experiments. Figure 13 shows the fast Fourier transform (FFT) of the same signals that were conditionally averaged in figure 9(*a*). The simulated signals with different levels of fast-ion diffusion have very similar shapes in the time domain, so their phase dependence is very similar. In the time domain, the experimental waveform differs markedly from the others; this difference appears in the FFT as a significant difference in the phase of the second and fourth harmonics. In general, for fast-ion signals in the presence of a strong source, the time evolution of $\nabla \cdot \tilde{\Gamma}$ provides more insight than the Fourier transform.

5. Error analysis

Having established that the divergence of the flux is the fundamental quantity for fast-ion perturbative experiments, the purpose of this section is to discuss and quantify the errors in $\nabla \cdot \tilde{\Gamma}$.

The ideal response of the system to a linear perturbation is symmetrical, with the signal during the negative cycle a mirror

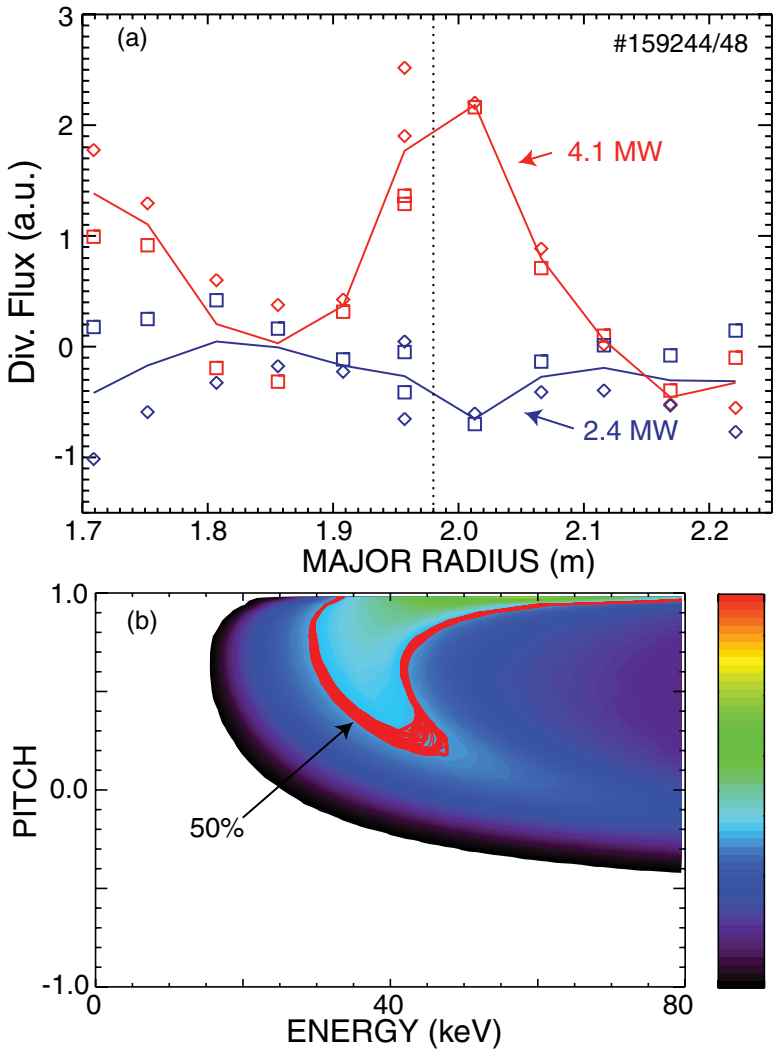

Figure 12. (*a*) Radial FIDA profile of $\langle \nabla \cdot \tilde{\gamma} \rangle$ from a discharge with significant (upper points and curve) and insignificant AE activity (lower points and curve). Diamond symbols represent the average value of $\nabla \cdot \tilde{\gamma}$ near the end of the positive cycle, square symbols represent the average value of $-\nabla \cdot \tilde{\gamma}$ near the end of the negative cycle, and the curves are the average of the two. (*b*) Velocity-space weight function versus energy and pitch $v_{\|}/v$ for the FIDA channel at $R = 2.01$ m for signals integrated between 651.8–653.3 nm. The linear color scale shown on the right is employed. The weight function is zero in the region below and to the left of the black curve. The lines represent the 50% contour of the weight function at 41 different times between 519–879 ms.

image of the signal in the positive cycle. If this is the case, the divergence of the flux in the positive cycle is equal and opposite to the divergence of the flux in the negative cycle, $\nabla \cdot \tilde{\Gamma}_+ = -\nabla \cdot \tilde{\Gamma}_-$. In practice, this ideal is not achieved in the DIII-D AE experiments. For example, for the points inside $R < 2.08$ m in figure 12(*a*), the data during the positive cycle in the plasma with strong AE activity are, on average, 67% larger than the data during the negative cycle. Similarly, for the case shown in figure 8(*c*), $\nabla \cdot \tilde{\Gamma}_+ \simeq 1.6|\nabla \cdot \tilde{\Gamma}_-|$. To investigate the source of this asymmetry, figure 14 plots five conditionally averaged signals that would be constant in an ideal experiment. The electron temperature does approach this ideal, with essentially no systematic variation during the cycle. Since the slowing-down time is comparable to the modulation period and the modulated beam only constitutes 20% of the total injected power, this weak variation is expected. The electron density exhibits a slight ($\lesssim$1%) variation, probably attributable to beam fuelling. The change in FIDA background light is larger, a few percent. However, since the active signal is only $\lesssim$20% of the total, the effect on the modulated signal is greater, a potential variation of $O(10\%)$. The biggest change is in the amplitude of AE activity, a $\sim$15% change. Apparently, ions from the modulated source drive the AEs harder; as a result, since the modes are stronger, the fast-ion transport is larger at the end of the positive cycle than at the end of the negative cycle (Analysis of discharges at differing DC power levels show that the AE amplitude modulation is largest for intermediate powers of 3–7 MW.). In principle, this departure from linearity could be reduced by modulating a lower-power beam but this would come at the expense of the signal-to-noise ratio.

Motion of the flux surfaces in response to the modulation is another potential complication. Flux-surface motion can reversibly advect fast ions through the spatial volume interrogated by the diagnostic. For example, for a radial displacement ΔR, the density in the interrogated volume will change

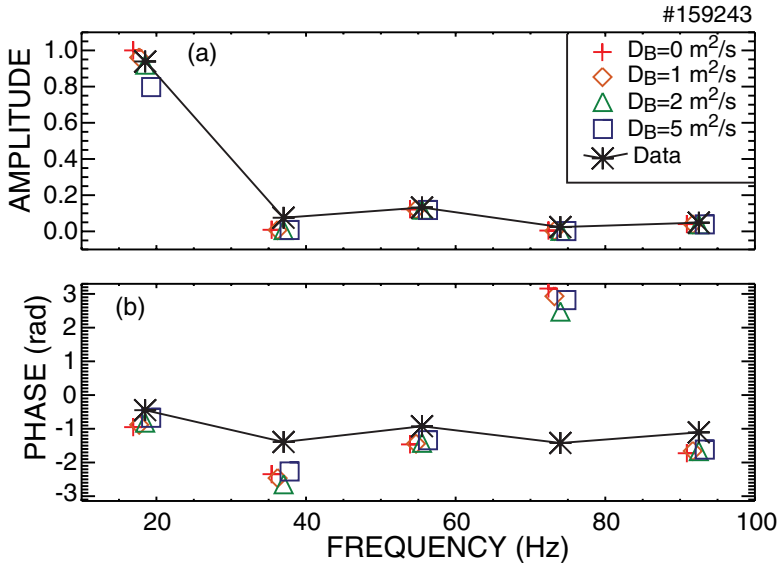

Figure 13. (*a*) Amplitude and (*b*) phase from the FFT of measured (∗) and simulated neutron signals with $D_B = 0$ (+), 1 (◊), 2 (△), and 5 $m^2\ s^{-1}$ (□). The corresponding conditionally-averaged signals appear in figure 9. A negative value of phase means the signal lags the source. (Note: the points are displaced slightly in frequency for clarity.)

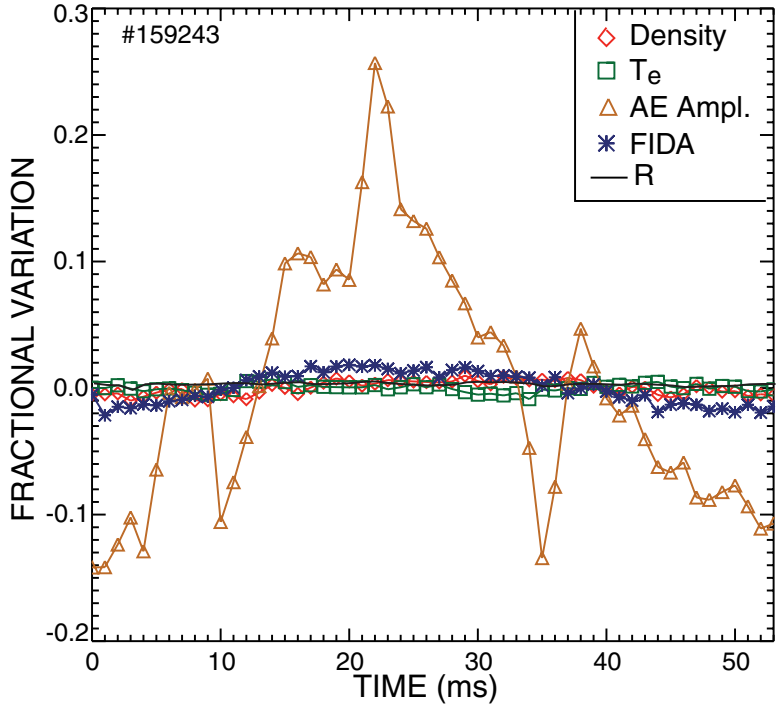

Figure 14. Detrended and conditionally-averaged fractional variation in the line-averaged electron density (◊), central electron temperature (□), AE amplitude (△), flux-surface motion (line without symbols) and FIDA background (∗) for the channel at $R = 1.96$ m in the discharge shown in figure 8(*c*). The FIDA background is from integration of the spectral region between 650.8–651.8 nm, where the active signal is negligible. The radial flux-surface motion is inferred from motional stark effect (MSE) data near the magnetic axis.

by $\Delta n \simeq \Delta R(\partial n/\partial R)$ during the cycle. Since the goal of the experiment is to measure *irreversible* transport processes, periodic variations associated with advection complicate the interpretation of the measured $\nabla \cdot \tilde{\Gamma}$. For the case shown in figure 14, the conditionally-averaged motion of a flux surface near the magnetic axis is only a few millimeters, so this effect is small but, in general, this effect is potentially important.

Another potential source of error in $\nabla \cdot \tilde{\Gamma}$ is associated with the theoretical waveform that provides the source and sink. Owing to averaging in the calculation of the distribution function, the theoretical waveform may not be on the identical time base as the experimental data. Slight timing offsets of <1 ms can alter the determination of $\tilde{S}_0$ and τ, ultimately changing the inferred $\nabla \cdot \tilde{\Gamma}$. Figure 15 shows an example of

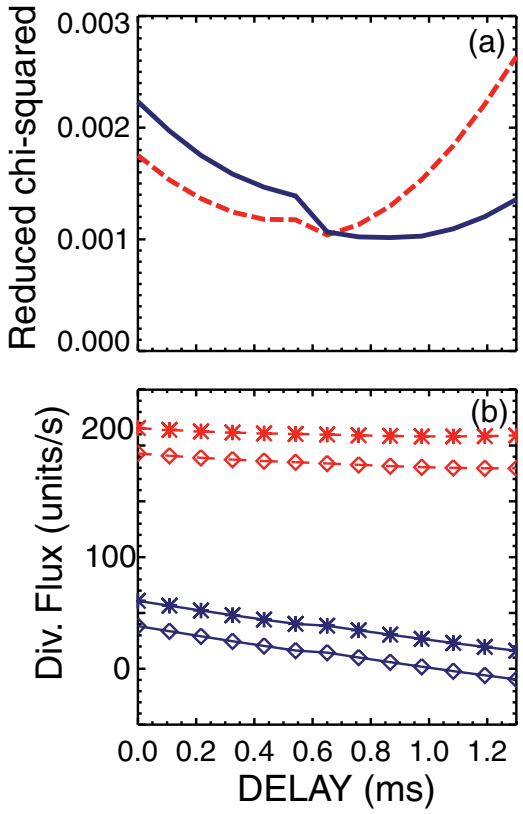

Figure 15. (*a*) Reduced chi-squared of the fit to the model solution equation (7) as a function of the offset δt between the experimental and theoretical time base for TRANSP/FIDASIM calculations of the expected NPA signal for the on-axis (solid) and off-axis (dashed) cases shown in figure 11(*b*). (*b*) Effect of δt on the inferred $\nabla \cdot \tilde{\Gamma}$.

Table 1. Sensitivity of $\nabla \cdot \tilde{\Gamma}/\tilde{S}_0$ in discharge #159243 to artificial enhancement of the density or temperature profile by 10%.

Diagnostic	n_e variation (%)	T_e variation (%)
Neutron	4.2	5.1
NPA	7.0	9.4
FIDA (2.01 m)	5.8	4.1

this effect on the divergence of flux inferred from an NPA signal. The best agreement of the model equation (equation (7)) to the waveform predicted by NUBEAM and FIDASIM is for an adjustment in time base of $\delta t \simeq 0.5$ ms. If the time base is not properly adjusted an error of 10% or more is easily incurred. By selecting an offset that provides the best agreement to the model equation, the likely error associated with this effect is $\lesssim$10%.

In general, due to the strong sensitivity of the inferred $\nabla \cdot \tilde{\Gamma}$ to the source and sink, errors in plasma parameters such as T_e and n_e can cause large errors; however, if a reference shot is available, systematic calibration errors largely cancel. To test this assertion, data from a discharge with appreciable AE activity is reanalyzed using artifically rescaled profiles of T_e and n_e. The results appear in table 1. Systematic enhancement of T_e and n_e by 10% cause $\sim$ 5% errors in $\nabla \cdot \tilde{\Gamma}/\tilde{S}_0$. If the normalization of equation (11) is omitted, as would be necessary in the absence of a reference shot, the neutron error doubles.

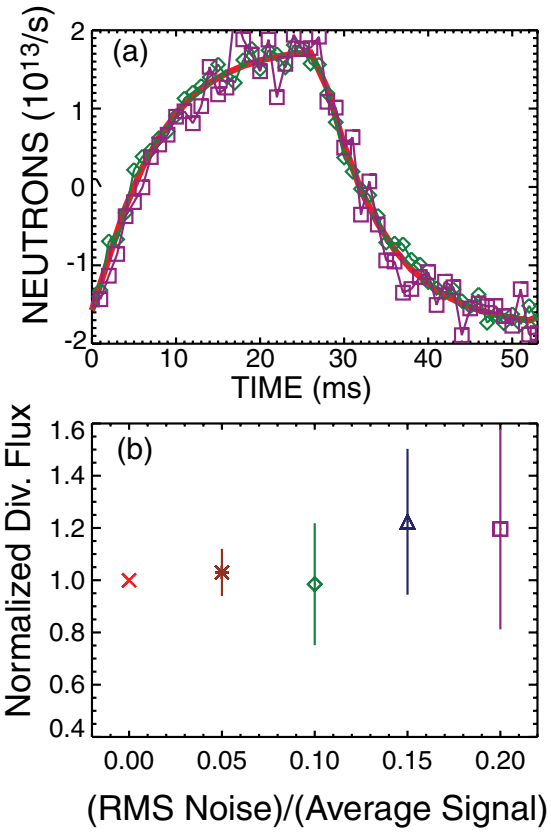

Figure 16. Effect of noise in the signal on the accuracy of the inferred $\nabla \cdot \tilde{\Gamma}$. Gaussian noise is added to the model $D_B = 5$ m^2 s^{-1} neutron signal shown in figure 9(*a*). (*a*) Representative signals with no (solid), 0.1 (◊), and 0.20 (□) RMS noise. (*b*) Average and standard deviation of $\nabla \cdot \tilde{\Gamma}$ for ten signals with the assumed RMS noise level.

In most cases, the contribution of plasma-parameter calibration errors to the overall error is modest.

Errors in the weight functions have an indirect impact. In the procedure described here, the source and sink terms are inferred from forward modeling using FIDASIM, so the weight functions themselves are not directly employed. On the other hand, if the diagnostic sensitivity is misrepresented, conclusions concerning the portion of phase space affected by an instability will be erroneous.

Random noise in the conditionally-averaged signal is a major source of error. To assess this effect, Gaussian noise at different levels is added to the very smooth waveform predicted by TRANSP in the presence of large $D_B = 5$ m^2 s^{-1} spatially-uniform diffusion. For each noise level, an ensemble of 10 different waveforms is created and analyzed. Typical conditionally-averaged signals for different noise levels appear in figure 16(*a*). The effect of the noise on the inferred values of $\nabla \cdot \tilde{\Gamma}$ appear in figure 16(*b*). For an RMS noise level of 5%, which is typical for the neutron signals in the DIII-D AE experiment, the standard deviation of the inferred $\nabla \cdot \tilde{\Gamma}$ varies by 8%. For an RMS noise level of 15%, which is typical for weaker FIDA signals in the DIII-D AE experiment, the standard deviation of the inferred $\nabla \cdot \tilde{\Gamma}$ varies by 31%. Evidently, a large signal-to-noise ratio is a prerequisite for accurate measurements of the fast-ion transport.

A convenient estimate of the uncertainty is provided by the MHD-quiescent reference discharges since, by assumption, these discharges have zero transport. In figure 8(*b*), the standard deviation and offset of $\nabla \cdot \tilde{\Gamma}$ are $\sim 0.1\tilde{S}_0$. In figure 12, the offset and standard deviation of $\nabla \cdot \tilde{\Gamma}$ in the reference shot are -11% and 17% of the largest point in the measured profile, implying that, for many positions, the error approaches 100% of the signal.

6. Conclusion

The data and analysis of the previous sections support the following conclusions concerning the design and interpretation of a perturbative fast-ion transport experiment.

1. The phase-space sensitivity of the diagnostic (its weight function W) is crucial to the interpretation of the results. Happily, W is accurately known for all of the standard fast-ion diagnostics.
2. Typically, the neutral-beam source makes a major contribution to the measured signal. Since the atomic physics of beam deposition is well understood, the contribution of the source to the signal is known accurately.
3. Thermalizing fast ions that escape the phase-space volume interrogated by the diagnostic also make a major contribution. Perhaps surprisingly, it is empirically demonstrated that the simple expression $\tilde{n}/\tau$ provides an accurate description of the thermalization sink even when the energy dependence of the weight function is nonmonotonic.
4. The fundamental measured quantity is the divergence of the flux from the diagnostically-weighted phase-space volume interrogated by the diagnostic, $\nabla \cdot \tilde{\Gamma}$ (equation (9)). In addition to spatial transport, this quantity can and does change due to transport in velocity space.
5. The procedure for evaluating equation (9) in a plasma with fast-ion transport is the following. (a) Measure the modulated signals in a discharge with negligible fast-ion transport. (b) Measure the modulated signals in the discharge with transport. (c) Calculate the expected signals in both discharges in the absence of transport. (d) Detrend and conditionally average all signals. (e) Use equation (7) to find τ and $\tilde{S}_0$ for the two theoretical cases and for the MHD-quiescent experimental case. In the fitting to the theoretical cases, make slight adjustments to the time base to optimize the fit. (f) Evaluate equation (9) using normalized values of τ and $\tilde{S}_0$ (equations 10 and 11); this eliminates the sensitivity to errors in the absolute calibration of the fast-ion and plasma profile diagnostics.
6. The temporal evolution of $\nabla \cdot \tilde{\Gamma}$ during the modulation pulse depends upon the transport mechanism. Accordingly, accurate measurements can provide a sensitive validation test for theories of fast-ion transport.
7. A good choice for the modulation period is $T \gtrsim \tau_s$. Transport on time scales much longer than τ_s is difficult to detect due to the importance of the thermalization term; moreover, an ion that has already delivered the bulk of its energy to the plasma is of limited interest for fusion applications.
8. The measured $\nabla \cdot \tilde{\Gamma}$ depends sensitively upon the portion of phase space populated by the modulated beam. Accordingly, it is desirable to populate orbits where strong interaction with the instability is anticipated. The differences in response for different sources can provide a second sensitive test for theory.
9. As in all perturbative experiments, the optimal strength of the source involves a trade-off between a strong source for improved signal-to-noise and a weak source for a better approximation to linearity. Strong evidence for non-linearity is observed in the DIII-D AE experiment.
10. Errors in the calculated value of $\nabla \cdot \tilde{\Gamma}$ can be substantial, especially for diagnostics that interrogate small volumes in phase space. The NPA diagnostic used here is a high bandwidth solid-state NPA operated in current mode and the FIDA diagnostic is a high throughput system; both diagnostics have relatively large collection volumes of ~ 5 cm diameter in the active beam. Even so, estimates suggest that the error in $\nabla \cdot \tilde{\Gamma}$ for a case with strong AE-induced transport is $\sim$20% for the NPA measurement and even larger for the weaker FIDA channels.

In conclusion, if adequate signal-to-noise and plasma stationarity can be achieved, perturbative studies provide a powerful technique to probe phase-space details of fast-ion transport by instabilities.

Acknowledgments

This material is based upon work supported by the U.S. Department of Energy, Office of Science, Office of Fusion Energy Sciences, using the DIII-D National Fusion Facility, a DOE Office of Science user facility, under Award DE-FC02-04ER54698. We thank the entire DIII-D team for their support. DIII-D data shown in this paper can be obtained in digital format by following the links at http://fusion.gat.com/global/D3D_DMP.

References

[1] Lopes Cardozo N.J. 1995 *Plasma Phys. Control. Fusion* **37** 799
[2] Ryter F., Dux R., Mantica P. and Tala T. 2010 *Plasma Phys. Control. Fusion* **52** 124043
[3] Deboo J.C. *et al* 2012 *Phys. Plasma* **19** 082518
[4] Collins C.S. *et al* 2016 *Phys. Rev. Lett.* **116** 095001
[5] Heidbrink W.W. *et al* 2007 *Phys. Rev. Lett.* **99** 245002
[6] Salewski M. *et al* 2011 *Nucl. Fusion* **51** 083014
[7] Salewski M. *et al* 2014 *Plasma Phys. Control. Fusion* **56** 105005
[8] Jac obsen A.S. *et al* 2014 *Rev. Sci. Instrum.* **85** 11E103
[9] Salewski M. *et al* 2012 *Nucl. Fusion* **52** 103008
[10] Geiger B. *et al* 2015 *Nucl. Fusion* **55** 083001
[11] Weiland M. *et al* 2016 *Plasma Phys. Control. Fusion* **58** 025012
[12] Fisch N.J. and Kritz A.H. 1990 *Phys. Fluids* B **2** 1486
[13] Gentle K.W. 1988 *Phys. Fluids* **31** 1105

[14] Muscatello C.M., Heidbrink W.W., Taussig D. and Burrell K.H. 2010 *Rev. Sci. Instrum.* **81** 10D316
[15] Zhu Y.B., Bortolon A., Heidbrink W.W., Celle S.L. and Roquemore A.L. 2012 *Rev. Sci. Instrum.* **83** 10D304
[16] Heidbrink W.W., Taylor P.L. and Phillips J.A. 1997 *Rev. Sci. Instrum.* **68** 536
[17] Strachan J.D. *et al* 1981 *Nucl. Fusion* **21** 67
[18] He idbrink W.W. *et al* 2003 *Nucl. Fusion* **43** 883
[19] Pankin A., Mccune D., Andre R., Bateman G. and Kritz A. 2004 *Comput. Phys. Commun.* **159** 157
[20] Heidbrink W.W., Liu D., Luo Y., Ruskov E. and Geiger B. 2011 *Commun. Comput. Phys.* **10** 716
[21] Sattin F., Escande D.F., Auriemma F., Urso G. and Terranova D. 2014 *Plasma Phys. Control. Fusion* **56** 114008